

# Charge-to-spin conversion at argon ion milled SrTiO<sub>3</sub>/NiFe hetero-interfaces

Cite as: Appl. Phys. Lett. **126**, 032401 (2025); doi: [10.1063/5.0238345](https://doi.org/10.1063/5.0238345)

Submitted: 11 September 2024 · Accepted: 6 January 2025 ·

Published Online: 22 January 2025



View Online



Export Citation



CrossMark

Amrendra Kumar,<sup>1</sup> Utkarsh Shashank,<sup>2,3</sup> Suman Kumar Maharana,<sup>1</sup> John Rex Mohan,<sup>2</sup> Joseph Vimal Vas,<sup>4,5</sup> Surbhi Gupta,<sup>6</sup> Hironori Asada,<sup>7</sup> Rafal E. Dunin-Borkowski,<sup>8,9</sup> Yasuhiro Fukuma,<sup>2,10,a)</sup> and Rohit Medwal<sup>1,a)</sup>

## AFFILIATIONS

<sup>1</sup>Department of Physics, Indian Institute of Technology Kanpur, Kanpur 208016, India

<sup>2</sup>Department of Physics and Information Technology, Faculty of Computer Science and Systems Engineering, Kyushu Institute of Technology, 680-4 Kawazu, Iizuka 820-8502, Japan

<sup>3</sup>Department of Physics, University of Gothenburg, Origovägen 6 B, 412 96 Gothenburg, Sweden

<sup>4</sup>Laboratory for in situ and operando Electron Nanoscopy, School of Material Science and Engineering, Nanyang Technological University, Singapore 637616, Singapore

<sup>5</sup>MajuLab, International Research Laboratory IRL 3654. CNRS, Université Côte d'Azur, Sorbonne Université, National University of Singapore, Nanyang Technological University, Singapore

<sup>6</sup>Department of Physics, Motilal Nehru National Institute of Technology, Barrister Mullah Colony, Teliarganj, Prayagraj, Uttar Pradesh 211004, India

<sup>7</sup>Division of Applied Science, Graduate School of Sciences and Technology for Innovation, Yamaguchi University, Yamaguchi 753-8511, Japan

<sup>8</sup>Ernst Ruska-Centre for Microscopy and Spectroscopy with Electrons, Forschungszentrum Jülich GmbH, Jülich 52425, Germany

<sup>9</sup>Institut für Experimentalphysik IV E, RWTH Aachen University, Aachen 52056, Germany

<sup>10</sup>Research Center for Neuromorphic AI hardware, Kyushu Institute of Technology, Kitakyushu 808-0196, Japan

<sup>a)</sup>Authors to whom correspondence should be addressed: [fukuma@phys.kyutech.ac.jp](mailto:fukuma@phys.kyutech.ac.jp) and [rmedwal@iitk.ac.in](mailto:rmedwal@iitk.ac.in)

## ABSTRACT

Two-dimensional electron gases (2DEGs) at perovskite oxide interfaces, such as strontium titanate (STO), have garnered significant attention due to their induced ferromagnetic (FM), spin-orbit coupling, and superconducting properties. The 2DEG, formed at the interface between STO and either insulating oxides or reactive metals, exhibits efficient charge-to-spin interconversion in STO/NM(non-magnetic)/FM structures. The insulating oxide layer at the STO interface attenuates the spin currents injected into the ferromagnet. In contrast, the metallic layers facilitate efficient spin current injection but suffer from spin current diffusion. Here, we present an approach to overcome these challenges by directly creating a 2DEG at the STO surface through Ar<sup>+</sup> ion bombardment. This method enables efficient spin-to-charge conversion without an intermediate NM layer. Our experimental and simulation results demonstrate the generation of unconventional spin currents at the STO(Ar<sup>+</sup>)/NiFe (Permalloy) interface. Our findings may enable applications of complex oxide and ferromagnet interfaces for efficient charge-to-spin conversion, paving the way for low-power, room-temperature oxide-based spintronic devices.

Published under an exclusive license by AIP Publishing. <https://doi.org/10.1063/5.0238345>

Oxide interfaces with spin degeneracy due to the band splitting into up- and down-spin bands are promising materials for efficient spin-to-charge interconversion.<sup>1</sup> This spin-dependent band splitting lies at the core of multiple phenomena in condensed matter physics, such as spin-to-charge conversion and charge-to-spin conversion. These oxide interfaces exhibit intriguing properties such as large

spin-orbit coupling, induced magnetism, and superconductivity.<sup>2-7</sup> Perovskite oxides, particularly strontium titanate (STO), at a two-dimensional hetero-interface, offers giant charge-to-spin conversion.<sup>8-13</sup> The STO interface facilitates the formation of two-dimensional electron gas (2DEG) through the deposition of oxides like AlO<sub>x</sub> and LaAlO<sub>3</sub> (LAO), or by deposition of reactive metals like Al,

Ta, and Y.<sup>8,14–16</sup> At the interface, titanium (Ti) has an accessible mixed valency, existing in both the  $Ti^{4+}$  and  $Ti^{3+}$  oxidation states. In a STO/LAO system, the 2DEG originates from the charged  $AlO_2^-$  surface of LAO, terminating on a charge neutral SrO surface of STO. For STO/metal interfaces, the formation of 2DEG is attributed to appearance of  $Ti^{3+}$  states. The 2DEG at both the STO/LAO interface and the STO/metal interface enables active gate-controlled tuning of spin-to-charge current. This phenomenon arises due to the absence of spatial inversion symmetry at the interface, which induces an electric field ( $\vec{E}$ ).<sup>17</sup> The electrons in the 2DEG carrying a momentum ( $\vec{p}$ ) interact with the  $\vec{E}$  and in their rest frame, experience an effective field  $\vec{P} \times \vec{E}$ .<sup>17–24</sup> In the presence of this effective field, the 2DEG showcases potential for a spin current.<sup>25</sup>

Recent spin transport studies on STO/NM/FM interfaces have demonstrated the potential of charge-to-spin current conversion facilitated by the 2DEG present at STO/LAO and  $AlO_x$  interfaces, as well as STO interfaces with metals such as Al, Ta, and Y. However, the insulating nature of  $AlO_x$  and LAO attenuates the direct propagation of spin current, thereby constraining the full potential of the 2DEG at the STO interface.<sup>15,26,27</sup> In contrast, metallic layers enable efficient spin current injection but are constrained by spin current diffusion.<sup>14,28,29</sup>

To address these challenges, recent research has focused on the induction of oxygen vacancies at the STO surface through  $Ar^+$  bombardment, which breaks the oxygen bonds and enhances vacancy formation, thus facilitating 2DEG formation on the STO surface.<sup>30–34</sup> By modulating the  $Ar^+$  exposure time, it is possible to transition the STO surface state between insulating, semiconducting, and metallic phases.

In our study, we utilized  $Ar^+$  milling to create oxygen vacancies on the STO surface, resulting in the formation of a 2DEG. We measured charge-to-spin conversion at the STO( $Ar^+$ )/NiFe interface using the spin torque ferromagnetic resonance (ST-FMR) technique, without the need for an intermediate NM layer. The conversion was mediated directly through the 2DEG present on the STO surface. Our STO( $Ar^+$ )/NiFe ST-FMR spectra were compared with the archetypal Pt/NiFe results, revealing the breaking of twofold ( $180^\circ + \phi$ ) and mirror ( $180^\circ - \phi$ ) symmetry of spin torques. These experimental results were further confirmed by micromagnetic simulations. Our findings demonstrate a straightforward and effective method for generating charge-to-spin current at the STO/NiFe interface, offering significant advancements for oxide spintronics applications.

The conducting surface of STO was created using the ion milling process. We used an ion gun to generate a beam of highly energetic ions (typically noble gases like  $Ar^+$  ions), which are then bombarded on the STO surface (see the [supplementary material S1](#)). The bombardment of  $Ar^+$  ions on the surface of STO with orientation (100) builds a conducting surface state by removing oxygen ions from STO, as shown in [Fig. 1\(a\)](#). The choice of inert gas helps us to prevent STO from additional impurities. The number of broken oxygen bonds on the STO surface is expected to increase rapidly with an increasing ion milling time. After confirming the formation of conducting surface states (see the [supplementary material S2](#)), ferromagnetic layer NiFe(5 nm) was deposited on ion milled STO( $Ar^+$ ) using DC sputtering. The designed STO( $Ar^+$ )/NiFe stack was subjected to microdevice fabrication using the photolithography technique for spin transport measurement (see the [supplementary material S1](#)).

We measure the thickness of the 2DEG by employing atomically resolved high-angle annular dark-field (HAADF) scanning

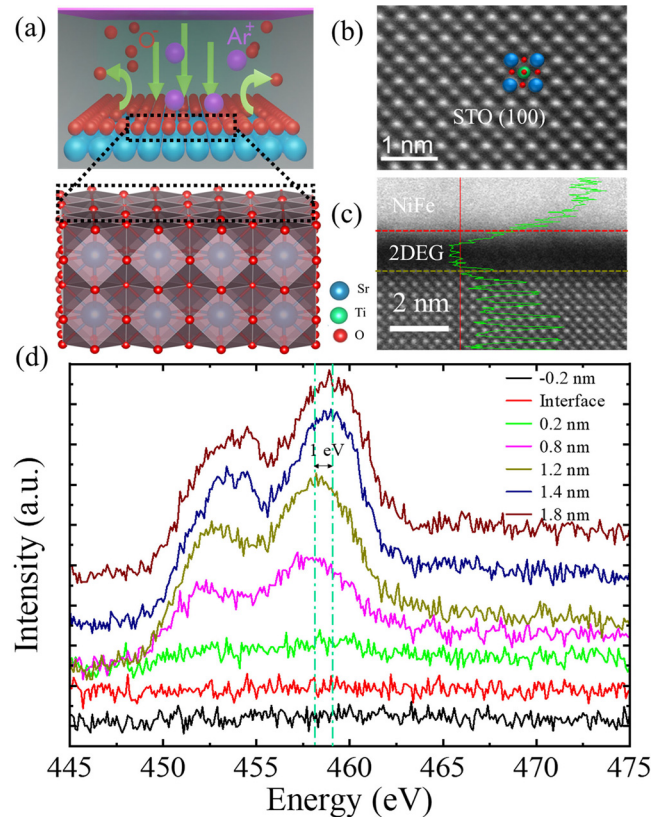


**FIG. 1.** (a) Schematic showing ( $Ar^+$ ) ion milling in the STO substrate. (b) Cross-sectional STEM showing the overlapped atomic model and the highlighted Sr (navy blue), Ti (cyan green), and O (red) atomic positions for STO(100). (c) Cross-sectional STEM image showing the thickness of different layers of STO( $Ar^+$ )/NiFe, the line profile (green solid line) of intensity along the solid red line. (d) Comparison of EELS spectra between the bulk STO  $Ti - L_{2,3}$  edges (brown line), the STO  $Ti - L_{2,3}$  edges at the interface (red line), and STO  $Ti - L_{2,3}$  edges present between bulk STO and interface.

transmission electron microscopy (STEM) technique. This imaging technique also provides insights into the interface quality and elemental composition of the sample. The cross-sectional samples for the STEM measurements are prepared using a FEI make NanoLab 460F1 FIB-SEM. The high-resolution cross-sectional HAADF-STEM image of the STO (100) overlapped with atomic models of STO crystal structure, highlighting the atoms position of Sr, Ti, and O in the STO unit cell, is shown in [Fig. 1\(b\)](#). The cross-sectional STEM image, [Fig. 1\(c\)](#), shows the NiFe (top layer), 2DEG (dark middle layer), and STO lattice structure (bottom layer) [Figure 1\(d\)](#) shows a comparison of experimental  $Ti - L_{2,3}$ , EELS spectra for bulk STO (brown line),<sup>35</sup> and at the interface [dashed red line in [Fig. 1\(c\)](#)]. At the interface STO  $Ti - L_{2,3}$ , edges shift toward lower energy, indicating a reduction in the oxidation state of  $Ti^{4+}$  to lower oxidation states. The trend continues up to the interface, beyond which the  $Ti - L_{2,3}$  peak disappears within the bulk NiFe layer.<sup>36</sup> The thickness of the 2DEG is determined by measuring the energy shift of the  $Ti - L_{2,3}$  peak captured at 200 kV using FEI Titan 8-300kV STEM. The shift begins at the interface of the bulk STO

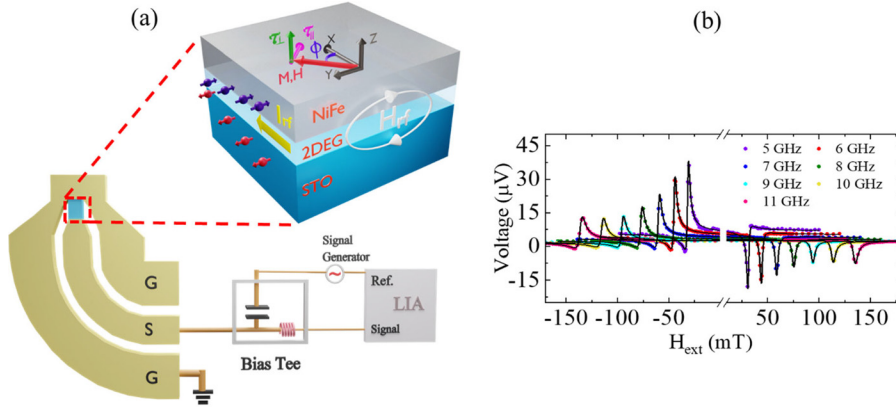


**FIG. 2.** (a) Schematic of ST-FMR measurement with lock-in setup to measure the  $V_{\text{mix}}$  voltage across the device. (b) Lorentzian fitting of  $V_{\text{mix}}$  voltage for 5–11 GHz frequency.

[dashed olive line in Fig. 1(c)] and completely disappears at 1.2 nm at the interface, indicating a 2DEG thickness of 1.2 nm.

After confirming the 2DEG at the STO(Ar<sup>+</sup>)/NiFe interface, we fabricated ST-FMR devices in the in-plane excitation geometry, as shown in Fig. 2(a), to perform the spin-dependent transport measurements.<sup>37,38</sup> The in-plane microwave charge current ( $I_{\text{rf}}$ ) was applied to the ST-FMR device in the ground-signal-ground (GSG) configuration. The applied  $I_{\text{rf}}$  exerted the Oersted field ( $H_{\text{rf}}$ ) on the magnetization vector of the ferromagnet. The applied  $I_{\text{rf}}$ , flowing through the 2DEG, also lead to the generation of spin current. The  $H_{\text{rf}}$  and generated spin current collectively drove magnetization precession under resonance conditions and lead to an oscillating resistance.<sup>39,40</sup>

The mixing of applied microwave current  $I_{\text{rf}}$  and oscillating resistance generated rectified DC voltage ( $V_{\text{mix}}$ ) across the device. A bias-tee was used to separate the AC and DC components of the signal, and the phase lock-in modulation technique was employed to measure the  $V_{\text{mix}}$  rectification DC voltage across the device using the lock-in amplifier (LIA) [see Fig. 2(a)]. The  $V_{\text{mix}}$  was measured at different frequencies,  $f$  ranging from 5 to 11 GHz as shown in Fig. 2(b). The amplitude of the  $V_{\text{mix}}$  decreased with increasing frequency due to a decrease in the precession cone angle of magnetization precession at a higher applied magnetic field value.<sup>41</sup> The observed rectifying voltage  $V_{\text{mix}}$  is deconvoluted in symmetric and antisymmetric Lorentzian components and is fitted using the following equation:<sup>37,40,42</sup>

$$V_{\text{mix}} = V_{\text{Sym}}F_{\text{Sym}}(H_{\text{ext}}) + V_{\text{Asym}}F_{\text{Asym}}(H_{\text{ext}}), \quad (1)$$

where  $F_{\text{Sym}}(H_{\text{ext}}) = \frac{(\Delta H)^2}{(H_{\text{ext}} - H_{\text{res}})^2 + (\Delta H)^2}$  is the symmetric part of the  $V_{\text{mix}}$  spectrum,  $F_{\text{Asym}}(H_{\text{ext}}) = \frac{\Delta H(H_{\text{ext}} - H_{\text{res}})}{(H_{\text{ext}} - H_{\text{res}})^2 + (\Delta H)^2}$  is the antisymmetric part,  $\Delta H$  and  $H_{\text{res}}$  are the half-width-at-half-maximum (linewidth) and the resonance field of ST-FMR spectra. The amplitude of the symmetric part of the spectra  $V_{\text{Sym}}$  mostly originates from in plane spin-orbit torque because of injection of spin current by SHE, and  $V_{\text{Asym}}$  is the amplitude of the antisymmetric part of the spectra, which originates from the Oersted field and Rashba-like field. The in-plane torque  $\tau_{\parallel}$  and out-of-plane torque  $\tau_{\perp}$  are proportional to symmetric  $V_{\text{Sym}}$  and antisymmetric  $V_{\text{Asym}}$  component of  $V_{\text{mix}}$ , which are given as the following equations:<sup>43</sup>

$$V_{\text{Sym}} = -\frac{I_{\text{rf}}}{2} \left( \frac{dR}{d\phi} \right) \frac{1}{\alpha\gamma(2H_{\text{res}} + 4\pi M_{\text{eff}})} \tau_{\parallel}, \quad (2)$$

$$V_{\text{Asym}} = -\frac{I_{\text{rf}}}{2} \left( \frac{dR}{d\phi} \right) \frac{\sqrt{1 + 4\pi M_{\text{eff}}/H_{\text{res}}}}{\alpha\gamma(2H_{\text{res}} + 4\pi M_{\text{eff}})} \tau_{\perp}, \quad (3)$$

where  $\phi$  is the in-plane angle between  $H_{\text{ext}}$  and the applied  $I_{\text{rf}}$  current, and  $\alpha$  and  $4\pi M_{\text{eff}}$  are Gilbert damping factor and effective magnetization of the ferromagnet. The symbol  $\gamma$  denotes the gyromagnetic ratio.<sup>44</sup> A typical  $V_{\text{mix}}$  of the STO(Ar<sup>+</sup>)/NiFe sample, as shown Fig. 3(a), has been measured at  $f = 5$  GHz at  $\phi = 45^\circ$ .<sup>37,45</sup> The  $H_{\text{res}}$  and  $\Delta H$  are estimated by fitting the measured  $V_{\text{mix}}$  signal for different  $f$  with Eq. (1). The variation of  $H_{\text{res}}$  as a function of  $f$  for STO(Ar<sup>+</sup>)/NiFe sample is plotted in Fig. 3(b). The  $4\pi M_{\text{eff}}$  is estimated using the following equation:

$$f = \frac{\gamma}{2\pi} \sqrt{(H_{\text{res}} + H_{\text{k}})(H_{\text{res}} + H_{\text{k}} + 4\pi M_{\text{eff}})}. \quad (4)$$

In this equation,  $H_{\text{k}}$  represents the effective in-plane magnetic anisotropy field and is set to 0 mT. The estimated values of  $4\pi M_{\text{eff}}$  and  $\frac{\gamma}{2\pi}$  are 951 mT and 0.0288 GHz/mT, respectively. Figure 3(c) shows that the linewidth broadening ( $\Delta H$ ) of ST-FMR spectra has a linear relationship with precessional frequency. The Gilbert damping parameter  $\alpha$ , which depends on linewidth  $\Delta H$ , is estimated using the linear function shown in the following equation:<sup>46,47</sup>

$$\Delta H = \Delta H_0 + \frac{2\pi f}{\gamma} \alpha. \quad (5)$$

Also,  $\Delta H_0$  is the inhomogeneous linewidth broadening, which is independent of  $f$ , and depends on the sample quality. The value of the Gilbert damping factor estimated is 0.007, which matches well with the previously reported value of 0.0084.<sup>48</sup>

It may be observed that the amplitude of the symmetric and antisymmetric spectra at opposite magnetic fields are different, as shown in Fig. 3(a). This difference in asymmetric voltage signal can arise due to (1) non-uniform microwave current flow in the devices and (2) an additional spin polarization configuration at the STO and NiFe interface.<sup>8,49,50</sup>

To understand this amplitude difference, we also fabricated Pt (5 nm)/NiFe (5 nm) devices in in-plane excitation geometry. We performed ST-FMR measurement at 5 GHz frequency [see the supplementary material S3, Fig. S3(a)], which shows that the symmetric ( $V_{\text{Sym}}$ ) and antisymmetric ( $V_{\text{Asym}}$ ) amplitude was the same at opposite magnetic fields. In this sample, the charge current along the x-direction generates spin polarization in the y-direction orthogonal to charge

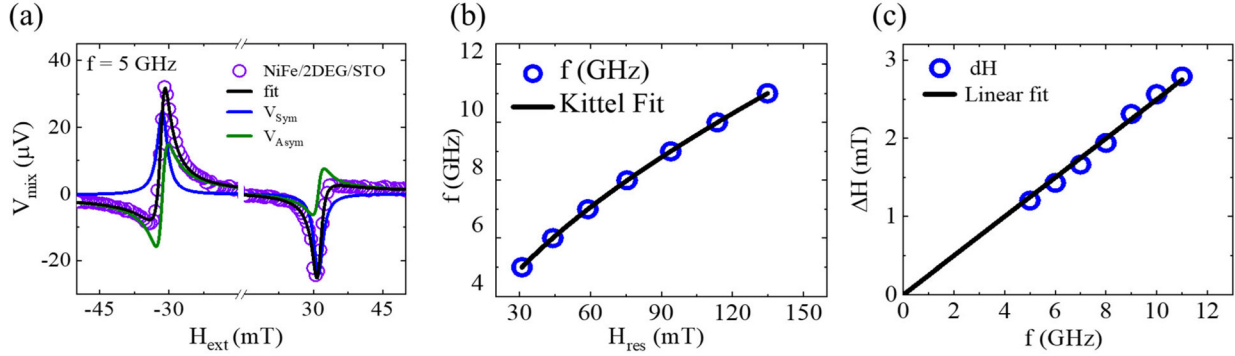


**FIG. 3.** (a) Lorentzian fitting of  $V_{\text{mix}}$  voltage for both negative and positive applied magnetic field at 5 GHz, where  $V_{\text{Sym}}$  and  $V_{\text{Asym}}$  represents the symmetric and antisymmetric part of the spectra. (b) Kittel fit of frequencies ranging from 5 to 11 GHz at  $\phi = 0^\circ$  and the corresponding  $4\pi H_{\text{eff}}$ . (c) Linear fitting of fullwidth half maxima with frequency.

current direction. The torques  $\vec{\tau}_\perp \propto \hat{m} \times \hat{y}$  and  $\vec{\tau}_\parallel \propto \hat{m} \times (\hat{m} \times \hat{y})$  are proportional to  $\cos(\phi)$ . The AMR depends on  $\cos^2(\phi)$  and appears as derivative of AMR, i.e.,  $\Delta(\text{AMR}) = \frac{d}{d\phi}(\cos^2(\phi)) \propto \sin(2\phi)$  leading to  $V_{\text{mix}} \propto \sin(2\phi)\cos(\phi)$ . This spin polarization configuration is referred to as conventional spin polarization. This symmetry occurs when the polarization  $\hat{p}$  of spin current and the rf field  $H_{\text{rf}}$  both are along the y axis and transverse to nonmagnetic (NM)/ferromagnetic (FM) interface,<sup>39,46</sup> resulting in  $V_{\text{mix}}(\phi) = -V_{\text{mix}}(\phi + 180^\circ)$ , eliminating the possible contribution due to non-uniform rf current distribution in the sample. To further investigate the contribution of spin polarization, in-plane angular-dependent (ST-FMR) measurements were performed with the applied external magnetic field ( $H_{\text{ext}}$ ) at 5 GHz. We have observed the amplitudes of both the symmetric and antisymmetric components, as shown in Fig. 4(a), follow a  $\sin(2\phi)\cos(\phi)$  dependence, consistent with AMR and torque dependencies. The similar ST-FMR device structure, as for Pt/NiFe, ensures proper microwave distribution in fabricated STO(Ar<sup>+</sup>)/NiFe ST-FMR devices.

To investigate the amplitude difference in symmetric and antisymmetric components of  $V_{\text{mix}}$  at opposite field values of  $H_{\text{ext}}$  in the

STO(Ar<sup>+</sup>)/NiFe sample, we performed angular dependent ST-FMR measurement at 5 GHz as shown in Fig. 4(b), respectively (see the supplementary material S4 for 7 GHz). The angular dependence of symmetric and antisymmetric voltage exhibits additional symmetry components beyond  $\sin(2\phi)\cos(\phi)$ , unlike Pt/NiFe. This results in the breaking of twofold ( $180^\circ + \phi$ ) and mirror symmetry ( $180^\circ - \phi$ ) and indicates the presence of additional torque components acting on the FM magnetization vector. These additional torques arise when  $\vec{p}$  and  $H_{\text{rf}}$  contain x and z components, and this spin polarization configuration is termed unconventional spin polarization.<sup>8</sup>

For unconventional cases, the symmetric component is fitted using the following equation:

$$V_{\text{Sym}} = S_{\text{DL}}^X \sin(2\phi)\sin(\phi) + S_{\text{DL}}^Y \sin(2\phi)\cos(\phi) + S_{\text{FL}}^Z \sin(2\phi), \quad (6)$$

where the  $S_{\text{DL}}^X$ ,  $S_{\text{DL}}^Y$ , and  $S_{\text{FL}}^Z$  are the weightage of  $\sin(2\phi)\sin(\phi)$ ,  $\sin(2\phi)\cos(\phi)$ , and  $\sin(2\phi)$  terms, respectively.<sup>51,52</sup> Similarly, the antisymmetric component is fitted using the following equation:

$$V_{\text{Asym}} = A_{\text{FL}}^X \sin(2\phi)\sin(\phi) + A_{\text{FL}}^Y \sin(2\phi)\cos(\phi) + A_{\text{DL}}^Z \sin(2\phi), \quad (7)$$

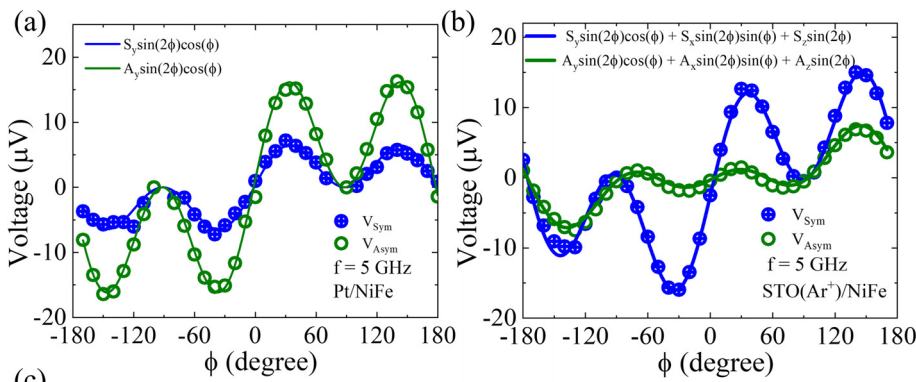


**FIG. 4.** In-plane angle-dependent ST-FMR measurements: (a) and (b) Extracted component from Lorentzian fitting of  $V_{\text{mix}}$  data for in-plane angle ( $\phi$ ) sweep. (a) Symmetric and antisymmetric components of  $V_{\text{mix}}$  and its fitted components for Pt/NiFe sample as a function of the in-plane angle between the applied  $H_{\text{rf}}$  and the external magnetic field  $H_{\text{ext}}$ . (b) Symmetric and antisymmetric components of  $V_{\text{mix}}$  and its fitted components for STO(Ar<sup>+</sup>)/NiFe samples as a function of ( $\phi$ ). (c) Table showing the voltage values percentage contribution in parentheses of different types of torques in symmetric and antisymmetric parts of  $V_{\text{mix}}$  voltage for Pt/NiFe and STO(Ar<sup>+</sup>)/NiFe samples, respectively.

sample	$f = 5$ GHz	$\sin(2\phi)\sin(\phi)$	$\sin(2\phi)\cos(\phi)$	$\sin(2\phi)$
Pt/NiFe	Symmetric	0	8.35 $\mu\text{V}$ (100 %)	0
	Antisymmetric	0	20.97 $\mu\text{V}$ (100 %)	0
STO(Ar <sup>+</sup> )/NiFe	Symmetric	3.63 $\mu\text{V}$ (16.79 %)	17.45 $\mu\text{V}$ (80.71 %)	0.54 $\mu\text{V}$ (2.50 %)
	Antisymmetric	0.26 $\mu\text{V}$ (2.93 %)	5.38 $\mu\text{V}$ (60.58 %)	3.24 $\mu\text{V}$ (36.49 %)

where the  $A_{\text{FL}}^X$ ,  $A_{\text{FL}}^Y$ , and  $A_{\text{DL}}^Z$  are the weightage of  $\sin(2\phi)\sin(\phi)$ ,  $\sin(2\phi)\cos(\phi)$ , and  $\sin(2\phi)$  terms, respectively.

The weightage of different components of the angular dependent symmetric and antisymmetric voltage, obtained for the STO(Ar<sup>+</sup>)/NiFe at 5 GHz and estimated from fitting using Eqs. (6) and (7), respectively, are shown in the table in Fig. 4(c). The symmetric component exhibits 16.79%  $\sin(2\phi)\sin(\phi)$  dependence, 80.71% arising from  $\sin(2\phi)\cos(\phi)$  dependence, with the remaining 2.50% arising from  $\sin(2\phi)$ . Meanwhile, the antisymmetric component has 2.93%, 60.58%, and 36.49% contributions from  $\sin(2\phi)\sin(\phi)$ ,  $\sin(2\phi)\cos(\phi)$ , and  $\sin(2\phi)$  dependence, respectively. In STO(Ar<sup>+</sup>)/NiFe, both symmetric and antisymmetric spectra show a significant presence of the  $\sin(2\phi)\sin(\phi)$  and  $\sin(2\phi)$  components. This is in sharp contrast to Pt/NiFe, where these components are absent due to spin Hall effect (SHE) in bulk Pt, which may cause conventional spin polarization.<sup>53</sup> The notable difference in spectra suggests the presence of strong unconventional spin-orbit coupling at the interface of STO and NiFe.

In our samples, we found that the Oersted field is dominant because amplitude  $A_{\text{FL}}^Y$  is large compared to its other counterparts, such as  $A_{\text{FL}}^X$  and  $S_{\text{FL}}^Z$  as shown in table Fig. 4(c). So, in this case, we use the value of  $A_{\text{FL}}^Y$  as a measure of the current density in the conducting surface of 2DEG; this allows us to quantify damping-like torque efficiencies per unit current density as follows:<sup>54,55</sup>

$$\zeta_{\text{DL},j}^X = \frac{S_{\text{DL}}^X}{A_{\text{FL}}^Y} \frac{e\mu_0 M_s t_{\text{NiFe}} t_{2\text{deg}}}{\hbar} \sqrt{1 + \frac{4\pi M_{\text{eff}}}{H_{\text{res}}}}, \quad (8a)$$

$$\zeta_{\text{DL},j}^Y = \frac{S_{\text{DL}}^Y}{A_{\text{FL}}^Y} \frac{e\mu_0 M_s t_{\text{NiFe}} t_{2\text{deg}}}{\hbar} \sqrt{1 + \frac{4\pi M_{\text{eff}}}{H_{\text{res}}}}, \quad (8b)$$

$$\zeta_{\text{DL},j}^Z = \frac{A_{\text{DL}}^Z}{A_{\text{FL}}^Y} \frac{e\mu_0 M_s t_{\text{NiFe}} t_{2\text{deg}}}{\hbar}. \quad (8c)$$

The effective magnetization  $4\pi M_{\text{eff}}$  is obtained from the Kittel fit, Eq. (4). The thicknesses  $t_{2\text{DEG}}$  and  $t_{\text{NiFe}}$  are 1.2 and 5 nm, respectively. The components  $S_{\text{DL}}^X$ ,  $S_{\text{DL}}^Y$ , and  $A_{\text{DL}}^Z$  and  $A_{\text{FL}}^Y$  are given in the table in Fig. 4(c). The term  $\zeta_{\text{DL},j}^Z$  does not contain the  $\sqrt{1 + \frac{4\pi M_{\text{eff}}}{H_{\text{res}}}}$  because both  $A_{\text{DL}}^Z$  and  $A_{\text{FL}}^Y$  are from the same antisymmetric component of the voltage  $V_{\text{Asym}}$ . Based on this, the estimated value of damping-like torques in different directions are as follows:  $\zeta_{\text{DL},j}^X = 0.033$ ,  $\zeta_{\text{DL},j}^Y = 0.16$ , and  $\zeta_{\text{DL},j}^Z = 0.006$ .

To better understand the spin polarization dependence of symmetric and antisymmetric components of the ST-FMR signal, we performed a simulation using MuMax<sup>3</sup>.<sup>56</sup> The simulation employs the Landau-Lifshitz-Gilbert equation that includes spin-orbit torques,<sup>37,57-59</sup>

$$\frac{d\vec{m}}{dt} = -\gamma\vec{m} \times \vec{B}_{\text{eff}} + \alpha\vec{m} \times \frac{d\vec{m}}{dt} + \frac{\gamma J_c(t)\hbar}{2e\tau_{\text{FM}}\mu_0 M_S} [\zeta_{\text{DL}}\vec{m} \times (\vec{\sigma} \times \vec{m}) + \zeta_{\text{FL}}\vec{m} \times \vec{\sigma}], \quad (9)$$

where  $\vec{m}$  and  $\vec{B}_{\text{eff}}$  are the normalized magnetization and the effective magnetic field, respectively.

The parameters  $\alpha$ ,  $\tau_{\text{FM}}$ , and  $\mu_0 M_S$  describe essential features of the ferromagnetic layer, representing the Gilbert damping factor, thickness, and saturation magnetization, which are crucial for understanding system behavior. The vectors  $(\vec{m} \times (\vec{\sigma} \times \vec{m}))$  and  $(\vec{\sigma} \times \vec{m})$  describe damping-like ( $\tau_{\text{DL}}$ ) and field-like ( $\tau_{\text{FL}}$ ) torques, respectively. Additionally, the dimensionless parameters  $\zeta_{\text{DL}}$  and  $\zeta_{\text{FL}}$  represent the efficiency of the  $J_c$  in generating ( $\tau_{\text{DL}}$ ) and ( $\tau_{\text{FL}}$ ), respectively.

We utilized 5 nm thick NiFe films with dimensions of  $80 \times 20 \mu\text{m}^2$ , replicating the aspect ratio of our ST-FMR device. Simulation parameters are given in the table in Fig. 5(b). We

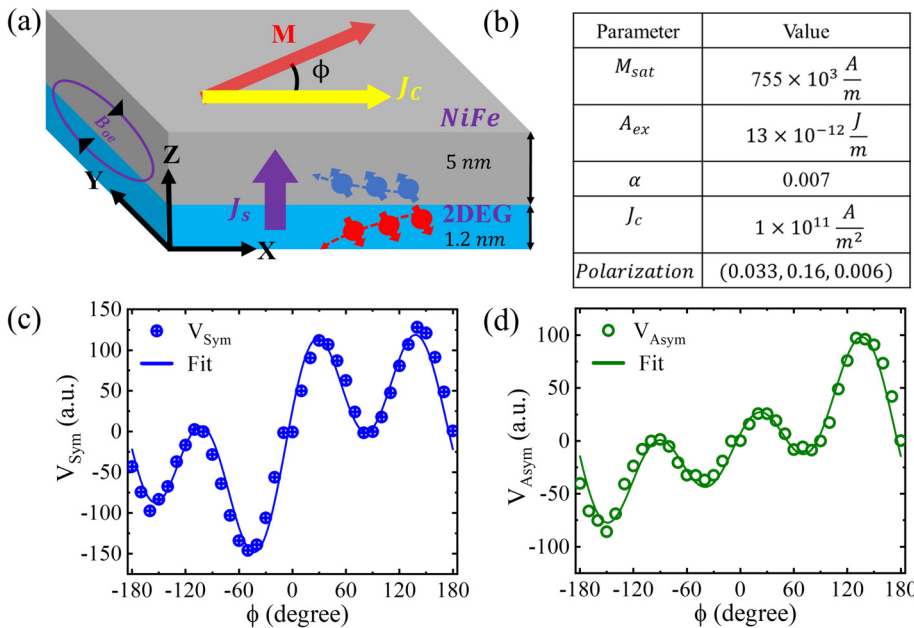


**FIG. 5.** In-plane angle-dependent ST-FMR data obtained from micromagnetic simulation: In-plane angle-dependent  $V_{\text{mix}}$  from ST-FMR simulation using MuMax<sup>3</sup> at 5 GHz. (a) Schematic showing the geometry of the sample, direction of charge current, spin current, and applied external magnetic field. (b) Table showing the parameters used in ST-FMR simulation. (c) Symmetric component with in-plane angle. (d) Antisymmetric component with in-plane angle.

conducted an ST-FMR simulation for the Pt/NiFe sample utilizing a conventional spin polarization model with the spin polarization (0, 1, 0) direction. Additionally, the  $\xi_{DL}$  and  $\xi_{FL}$  are set to 1 and 0, respectively (see the [supplementary material S5](#)). As in experiments, a charge current density  $J_c$  of  $1 \times 10^{11} \text{ A/m}^2$  is applied in the x-direction, which exerts a magnetic field ( $H_{rf}$ ) torque on the magnetization vector of NiFe. Additionally, the spin current generated from the  $J_c$  due to the SHE effect of Pt also exerts SOT on the magnetization vector of NiFe. The  $H_{rf}$  and generated spin current collectively drive the magnetization precession. We get the  $V_{mix}(\propto m_a)$  by fitting the spatial averaged magnetization amplitude  $m_y(t)$  with  $m_y(t) = m_a \cos(2\pi ft - \phi)$ .<sup>60</sup> Where  $m_y(t)$  is the instantaneous y component of the magnetization,  $m_a$  is the amplitude of the oscillation, and  $\phi$  is the phase delay between magnetization and the rf current. We have observed that both symmetric and antisymmetric components of  $V_{mix}$  spectra (see the [supplementary material S5](#)) exhibit a  $\sin(2\phi)\cos(\phi)$  dependence, as expected from our experimental findings.

As for the  $\text{STO}(\text{Ar}^+)/\text{NiFe}$  sample, we have simulated an unconventional spin polarization model. In this model, a current density  $J_c$  of  $1 \times 10^{11} \text{ A/m}^2$  is applied in the x-direction as shown in [Fig. 5\(a\)](#). We set the spin polarization vector to (0.033, 0.16, 0.006), as shown in the table in [Fig. 5\(b\)](#) with the  $\xi_{DL}$  and  $\xi_{FL}$  set to 1 and 0.14, respectively. The conducting 2DEG layer generates spin current from the charge current. The simulation reveals that the symmetric part of  $V_{mix}$  has additional terms  $\sin(2\phi)\sin(\phi)$  and  $\sin(2\phi)$ , arising due to damping-like torque in the x-direction and field-like torque in the z-direction as shown in [Fig. 5\(c\)](#). Similarly, for the antisymmetric part, there are additional terms  $\sin(2\phi)\sin(\phi)$  and  $\sin(2\phi)$ , which arise from the field-like torque in the x-direction and damping-like torque in the z-direction, as shown in [Fig. 5\(d\)](#). This additional dependence indicates that the presence of x and z components in spin polarization invites additional torques, so the symmetric and antisymmetric components of  $V_{mix}$  no longer shows the  $\sin(2\phi)\cos(\phi)$  dependence, as in the conventional polarization case of Pt/NiFe. The  $I_{rf}$  distribution is consistent between the two simulations; thus, this pronounced effect can be attributed to the anisotropic spin diffusion from  $\text{STO}(\text{Ar}^+)$  to the ferromagnetic layer.

In summary, our study demonstrates the effectiveness of ion milling and defect engineering in tailoring the spintronic properties of perovskite materials. The  $\text{Ar}^+$  milling at the STO surface breaks oxygen bonds, leading to the formation of a 2DEG and effectively transforming the STO surface from an insulator to a metallic state. Milling effectively bypasses the need for intermediate non-magnetic layers, addressing key challenges such as spin current attenuation and diffusion. The charge to spin conversion mediated through 2DEG results in unconventional spin polarized current at the  $\text{STO}(\text{Ar}^+)/\text{NiFe}$  interface. Furthermore, the angular-dependent analysis of the symmetric and antisymmetric components of the rectification voltage in ST-FMR spectra reveal the breaking of spin-orbit torque symmetries. The observation of unconventional spin current at the interface is further confirmed by the micromagnetic simulations, employing uniform current distribution, in both Pt/NiFe and  $\text{STO}(\text{Ar}^+)/\text{NiFe}$  samples. These findings pave the way for further exploration and development of oxide-based spintronics for future spin-electronic and computing technologies.

See the [supplementary material](#) for details on device fabrication, compositional mapping of the sample,  $\text{Ar}^+$  ion milling parameters,

ST-FMR measurements of Pt/NiFe samples. Furthermore, it includes angle-dependent ST-FMR data for the  $\text{STO}/2\text{DEG}/\text{NiFe}$  sample at 7 GHz RF frequency and simulation results for Pt/NiFe using MuMax<sup>3</sup>.

A.K. acknowledges support through PMRF. R.M. acknowledges the Initiation Grant, IIT Kanpur, the SERB Grant (Project No. SERB/PHY/20223613), and the I-HUB Quantum Technology Foundation, IISER Pune, for financial support. Y.F. and H.A. would like to acknowledge JSPS Grant-in-Aid (KAKENHI No. 22K04198), Iketani Science and Technology Foundation, Heiwa Nakajima Foundation and Meisenkai. S.K.M. and R.M. acknowledge the PARAM Sanganak facility at IIT Kanpur. The authors would like to acknowledge Arun Jacob Mathew, Akihisa Iwamoto, Kazuki Shintaku, and Soki Mizota for their help in resistivity measurements.

## AUTHOR DECLARATIONS

### Conflict of Interest

The authors have no conflicts to disclose.

### Author Contributions

**Amrendra Kumar:** Conceptualization (equal); Data curation (equal); Formal analysis (equal); Investigation (equal); Methodology (equal); Project administration (equal); Validation (equal); Visualization (equal); Writing – original draft (equal). **Utkarsh Shashank:** Conceptualization (equal); Data curation (equal); Formal analysis (equal); Investigation (equal); Methodology (equal); Project administration (equal); Validation (equal); Visualization (equal); Writing – review & editing (equal). **Suman Kumar Maharana:** Data curation (supporting); Formal analysis (supporting); Methodology (supporting); Validation (equal); Visualization (equal); Writing – review & editing (equal). **John Rex Mohan:** Methodology (equal); Validation (equal); Visualization (equal); Writing – review & editing (equal). **Joseph Vimal Vas:** Data curation (supporting); Resources (supporting); Validation (equal); Visualization (equal); Writing – review & editing (equal). **Surbhi Gupta:** Data curation (supporting); Supervision (equal); Validation (equal); Visualization (equal); Writing – review & editing (equal). **Hironori Asada:** Funding acquisition (equal); Project administration (equal); Resources (equal); Validation (equal); Visualization (equal); Writing – review & editing (equal). **R. E. Dunin-Borkowski:** Data curation (supporting); Resources (supporting); Validation (equal); Visualization (equal); Writing – review & editing (equal). **Yasuhiro Fukuma:** Conceptualization (equal); Funding acquisition (equal); Project administration (equal); Resources (equal); Software (equal); Supervision (equal); Validation (equal); Visualization (equal); Writing – review & editing (equal). **Rohit Medwal:** Conceptualization (equal); Data curation (supporting); Funding acquisition (lead); Project administration (lead); Resources (equal); Supervision (lead); Validation (equal); Visualization (equal); Writing – review & editing (equal).

## DATA AVAILABILITY

The data that support the findings of this study are available from the corresponding authors upon reasonable request.

## REFERENCES

- <sup>1</sup>W. Han, Y. Otani, and S. Maekawa, "Quantum materials for spin and charge conversion," *NPJ Quantum Mater.* **3**(1), 27 (2018).
- <sup>2</sup>Y.-L. Han, S.-C. Shen, J. You, H.-O. Li, Z.-Z. Luo, C.-J. Li, G.-L. Qu, C.-M. Xiong, R.-F. Dou, L. He, D. Naugle, G.-P. Guo, and J.-C. Nie, "Two-dimensional superconductivity at (110) LaAlO<sub>3</sub>/SrTiO<sub>3</sub> interfaces," *Appl. Phys. Lett.* **105**(19), 192603 (2014).
- <sup>3</sup>N. Reyren, S. Gariglio, A. D. Caviglia, D. Jaccard, T. Schneider, and J.-M. Triscone, "Anisotropy of the superconducting transport properties of the LaAlO<sub>3</sub>/SrTiO<sub>3</sub> interface," *Appl. Phys. Lett.* **94**(11), 112506 (2009).
- <sup>4</sup>K. Han, K. Hu, X. Li, K. Huang, Z. Huang, S. Zeng, D. Qi, C. Ye, J. Yang, H. Xu, A. Ariando, J. Yi, W. Lü, S. Yan, and X. R. Wang, "Erasable and recreatable two-dimensional electron gas at the heterointerface of SrTiO<sub>3</sub> and a water-dissolvable overlayer," *Sci. Adv.* **5**(8), eaaw7286 (2019).
- <sup>5</sup>H. Y. Hwang, Y. Iwasa, M. Kawasaki, B. Keimer, N. Nagaosa, and Y. Tokura, "Emergent phenomena at oxide interfaces," *Nat. Mater.* **11**(2), 103–113 (2012).
- <sup>6</sup>D. A. Dikin, M. Mehta, C. W. Bark, C. M. Folkman, C. B. Eom, and V. Chandrasekhar, "Coexistence of superconductivity and ferromagnetism in two dimensions," *Phys. Rev. Lett.* **107**(5), 56802 (2011).
- <sup>7</sup>L. Li, C. Richter, J. Mannhart, and R. C. Ashoori, "Coexistence of magnetic order and two-dimensional superconductivity at LaAlO<sub>3</sub>/SrTiO<sub>3</sub> interfaces," *Nat. Phys.* **7**(10), 762–766 (2011).
- <sup>8</sup>U. Shashank, A. Deka, C. Ye, S. Gupta, R. Medwal, R. S. Rawat, H. Asada, X. Renshaw Wang, and Y. Fukuma, "Room-temperature charge-to-spin conversion from quasi-2D electron gas at SrTiO<sub>3</sub>-based interfaces," *Phys. Status Solidi RRL* **17**(6), 2200377 (2023).
- <sup>9</sup>G. Herranz, F. Sánchez, N. Dix, M. Scigaj, and J. Fontcuberta, "High mobility conduction at (110) and (111) LaAlO<sub>3</sub>/SrTiO<sub>3</sub> interfaces," *Sci. Rep.* **2**(1), 758 (2012).
- <sup>10</sup>A. S. Everhardt, M. Mahendra, X. Huang, S. Sayed, T. A. Gosavi, Y. Tang, C.-C. Lin, S. Manipatruni, I. A. Young, S. Datta, J.-P. Wang, and R. Ramesh, "Tunable charge to spin conversion in strontium iridate thin films," *Phys. Rev. Mater.* **3**(5), 51201 (2019).
- <sup>11</sup>E. Lesne, Y. Fu, S. Oyarzun, J. C. Rojas-Sánchez, D. C. Vaz, H. Naganuma, G. Sicoli, J.-P. Attané, M. Jamet, E. Jacquet, J.-M. George, A. Barthélémy, H. Jaffrès, A. Fert, M. Bibes, and L. Vila, "Highly efficient and tunable spin-to-charge conversion through Rashba coupling at oxide interfaces," *Nat. Mater.* **15**(12), 1261–1266 (2016).
- <sup>12</sup>H. Yang, B. Zhang, X. Zhang, X. Yan, W. Cai, Y. Zhao, J. Sun, K. L. Wang, D. Zhu, and W. Zhao, "Giant charge-to-spin conversion efficiency in SrTiO<sub>3</sub>-based electron gas interface," *Phys. Rev. Appl.* **12**(3), 034004 (2019).
- <sup>13</sup>F. Zhang, J. Zhang, X. Chi, R. Hao, W. Chen, H. Yang, D. Zhu, Q. Zhang, W. Zhao, H. Zhang, and J. Sun, "Giant efficiency for charge-to-spin conversion via the electron gas at the LaTiO<sub>3+δ</sub>/SrTiO<sub>3</sub> interface," *Phys. Rev. B* **105**(19), 195110 (2022).
- <sup>14</sup>L. M. Vicente-Arche, S. Mallik, M. Cosset-Cheneau, P. Noël, D. C. Vaz, F. Trier, T. A. Gosavi, C.-C. Lin, D. E. Nikonov, I. A. Young, A. Sander, A. Barthélémy, J.-P. Attané, L. Vila, and M. Bibes, "Metal/SrTiO<sub>3</sub> two-dimensional electron gases for spin-to-charge conversion," *Phys. Rev. Mater.* **5**(6), 064005 (2021).
- <sup>15</sup>Y. Wang, R. Ramaswamy, M. Motapothula, K. Narayanapillai, D. Zhu, J. Yu, T. Venkatesan, and H. Yang, "Room-temperature giant charge-to-spin conversion at the SrTiO<sub>3</sub>-LaAlO<sub>3</sub> oxide interface," *Nano Lett.* **17**(12), 7659–7664 (2017).
- <sup>16</sup>A. Ohtomo and H. Y. Hwang, "A high-mobility electron gas at the LaAlO<sub>3</sub>/SrTiO<sub>3</sub> heterointerface," *Nature* **427**(6973), 423–426 (2004).
- <sup>17</sup>K. Gopinadhan, A. Annadi, Y. Kim, A. Srivastava, B. Kumar, J. Chen, J. M. D. Coey, Ariando, and T. Venkatesan, "Gate tunable in- and out-of-plane spin-orbit coupling and spin-splitting anisotropy at LaAlO<sub>3</sub>/SrTiO<sub>3</sub> (110) interface," *Adv. Electron. Mater.* **1**(8), 1500114 (2015).
- <sup>18</sup>J. C. R. Sánchez, L. Vila, G. Desfonds, S. Gambarelli, J. P. Attané, J. M. De Teresa, C. Magén, and A. Fert, "Spin-to-charge conversion using Rashba coupling at the interface between non-magnetic materials," *Nat. Commun.* **4**, 2944 (2013).
- <sup>19</sup>F. Hellman, A. Hoffmann, Y. Tserkovnyak, G. S. D. Beach, E. E. Fullerton, C. Leighton, A. H. MacDonald, D. C. Ralph, D. A. Arena, H. A. Dürr, P. Fischer, J. Grolier, J. P. Heremans, T. Jungwirth, A. V. Kimel, B. Koopmans, I. N. Krivorotov, S. J. May, A. K. Petford-Long, J. M. Rondinelli, N. Samarth, I. K. Schuller, A. N. Slavin, M. D. Stiles, O. Tchernyshyov, A. Thiaville, and B. L. Zink, "Interface-induced phenomena in magnetism," *Rev. Mod. Phys.* **89**(2), 025006 (2017).
- <sup>20</sup>J. Chen, K. Wu, W. Hu, and J. Yang, "Spin-orbit coupling in 2D semiconductors: A theoretical perspective," *J. Phys. Chem. Lett.* **12**(51), 12256–12268 (2021).
- <sup>21</sup>A. Manchon, H. C. Koo, J. Nitta, S. M. Frolov, and R. A. Duine, "New perspectives for Rashba spin-orbit coupling," *Nat. Mater.* **14**(9), 871–882 (2015).
- <sup>22</sup>S. Shi, A. Wang, Y. Wang, R. Ramaswamy, L. Shen, J. Moon, D. Zhu, J. Yu, S. Oh, Y. Feng, and H. Yang, "Efficient charge-spin conversion and magnetization switching through the Rashba effect at topological-insulator/Ag interfaces," *Phys. Rev. B* **97**(4), 041115 (2018).
- <sup>23</sup>J. Nitta, T. Akazaki, H. Takayanagi, and T. Enoki, "Gate control of spin-orbit interaction in an inverted In<sub>0.53</sub>Ga<sub>0.47</sub>As/In<sub>0.52</sub>Al<sub>0.48</sub>As heterostructure," *Phys. Rev. Lett.* **78**, 1335–1338 (1997).
- <sup>24</sup>R. Ohshima, Y. Ando, K. Matsuzaki, T. Susaki, M. Weiler, S. Klingler, H. Huebl, E. Shikoh, T. Shinjo, S. T. B. Goennenwein, and M. Shiraishi, "Strong evidence for d-electron spin transport at room temperature at a LaAlO<sub>3</sub>/SrTiO<sub>3</sub> interface," *Nat. Mater.* **16**(6), 609–614 (2017).
- <sup>25</sup>V. M. Edelstein, "Spin polarization of conduction electrons induced by electric current in two-dimensional asymmetric electron systems," *Solid State Commun.* **73**(3), 233–235 (1990).
- <sup>26</sup>Q. Song, H. Zhang, T. Su, W. Yuan, Y. Chen, W. Xing, J. Shi, J. Sun, and W. Han, "Observation of inverse Edelstein effect in Rashba-split 2DEG between SrTiO<sub>3</sub> and LaAlO<sub>3</sub> at room temperature," *Sci. Adv.* **3**(3), e1602312 (2017).
- <sup>27</sup>C. H. Du, H. L. Wang, Y. Pu, T. L. Meyer, P. M. Woodward, F. Y. Yang, and P. C. Hammel, "Probing the spin pumping mechanism: Exchange coupling with exponential decay in Y<sub>3</sub>Fe<sub>5</sub>O<sub>12</sub>/barrier/Pt heterostructures," *Phys. Rev. Lett.* **111**(24), 247202 (2013).
- <sup>28</sup>S. Zhang and A. Fert, "Conversion between spin and charge currents with topological insulators," *Phys. Rev. B* **94**(18), 184423 (2016).
- <sup>29</sup>H. He, L. Tai, H. Wu, D. Wu, A. Razavi, T. A. Gosavi, E. S. Walker, K. Oguz, C.-C. Lin, K. Wong, Y. Liu, B. Dai, and K. L. Wang, "Conversion between spin and charge currents in topological-insulator/nonmagnetic-metal systems," *Phys. Rev. B* **104**(22), L220407 (2021).
- <sup>30</sup>J.-W. Chang, J. S. Lee, T. H. Lee, J. Kim, and Y.-J. Doh, "Controlled formation of high-mobility shallow electron gases in SrTiO<sub>3</sub> single crystal," *Appl. Phys. Express* **8**(5), 055701 (2015).
- <sup>31</sup>L. Iglesias, A. Sarantopoulos, C. Magén, and F. Rivadulla, "Oxygen vacancies in strained SrTiO<sub>3</sub> thin films: Formation enthalpy and manipulation," *Phys. Rev. B* **95**(16), 165138 (2017).
- <sup>32</sup>Y. Li, S. N. Phattalung, S. Limpijumng, J. Kim, and J. Yu, "Formation of oxygen vacancies and charge carriers induced in the n-type interface of a LaAlO<sub>3</sub> overlayer on SrTiO<sub>3</sub>(001)," *Phys. Rev. B* **84**(24), 245307 (2011).
- <sup>33</sup>N. D. Browning, J. P. Buban, H. O. Moltaji, S. J. Pennycook, G. Duscher, K. D. Johnson, R. P. Rodrigues, and V. P. Dravid, "The influence of atomic structure on the formation of electrical barriers at grain boundaries in SrTiO<sub>3</sub>," *Appl. Phys. Lett.* **74**(18), 2638–2640 (1999).
- <sup>34</sup>Q. Wang, W. Zhang, W. Zhang, and H. Zeng, "In-situ monitor of insulator to metal transition in SrTiO<sub>3</sub> by Ar<sup>+</sup> irradiation," *Appl. Surf. Sci.* **365**, 84–87 (2016).
- <sup>35</sup>C. Cantoni, J. Gazquez, F. Miletto Granozio, M. P. Oxley, M. Varela, A. R. Lupini, S. J. Pennycook, C. Aruta, U. S. di Uccio, P. Perna, and D. Maccariello, "Electron transfer and ionic displacements at the origin of the 2D electron gas at the LAO/STO interface: Direct measurements with atomic-column spatial resolution," *Adv. Mater.* **24**(29), 3952–3957 (2012).
- <sup>36</sup>H. Tan, J. Verbeeck, A. Abakumov, and G. Van Tendeloo, "Oxidation state and chemical shift investigation in transition metal oxides by EELS," *Ultramicroscopy* **116**, 24–33 (2012).
- <sup>37</sup>L. Liu, T. Moriyama, D. C. Ralph, and R. A. Buhrman, "Spin-torque ferromagnetic resonance induced by the spin Hall effect," *Phys. Rev. Lett.* **106**(3), 036601 (2011).
- <sup>38</sup>L. Liu, C.-F. Pai, Y. Li, H. W. Tseng, D. C. Ralph, and R. A. Buhrman, "Spin-torque switching with the giant spin Hall effect of Tantalum," *Science* **336**(6081), 555–558 (2012).

- <sup>39</sup>M. Harder, Y. Gui, and C.-M. Hu, "Electrical detection of magnetization dynamics via spin rectification effects," *Phys. Rep.* **661**, 1–59 (2016).
- <sup>40</sup>D. MacNeill, G. M. Stiehl, M. H. D. Guimarães, R. A. Buhrman, J. Park, and D. C. Ralph, "Control of spin-orbit torques through crystal symmetry in WTe<sub>2</sub>/ferromagnet bilayers," *Nat. Phys.* **13**(3), 300–305 (2017).
- <sup>41</sup>S. Gupta, R. Medwal, D. Kodama, K. Kondou, Y. Otani, and Y. Fukuma, "Important role of magnetization precession angle measurement in inverse spin Hall effect induced by spin pumping," *Appl. Phys. Lett.* **110**(2), 022404 (2017).
- <sup>42</sup>G. M. Stiehl, D. MacNeill, N. Sivasdas, I. El Baggari, M. H. D. Guimarães, N. D. Reynolds, L. F. Kourkoutis, C. J. Fennie, R. A. Buhrman, and D. C. Ralph, "Current-induced torques with Dresselhaus symmetry due to resistance anisotropy in 2D materials," *ACS Nano* **13**(2), 2599–2605 (2019).
- <sup>43</sup>S. Karimeddiny and D. C. Ralph, "Resolving discrepancies in spin-torque ferromagnetic resonance measurements: Lineshape versus linewidth analyses," *Phys. Rev. Appl.* **15**(6), 064017 (2021).
- <sup>44</sup>C. Kittel, *Introduction to Solid State Physics* (John Wiley & Sons, Inc, 2005).
- <sup>45</sup>U. Shashank, R. Medwal, T. Shibata, R. Nongjai, J. V. Vas, M. Duchamp, K. Asokan, R. S. Rawat, H. Asada, S. Gupta, and Y. Fukuma, "Enhanced spin Hall effect in S-implanted Pt," *Adv. Quantum Technol.* **4**(1), 2000112 (2021).
- <sup>46</sup>U. Shashank, R. Medwal, Y. Nakamura, J. R. Mohan, R. Nongjai, A. Kandasami, R. S. Rawat, H. Asada, S. Gupta, and Y. Fukuma, "Highly dose dependent damping-like spin-orbit torque efficiency in O-implanted Pt," *Appl. Phys. Lett.* **118**(25), 252406 (2021).
- <sup>47</sup>U. Shashank, Y. Nakamura, Y. Kusaba, T. Tomoda, R. Nongjai, A. Kandasami, R. Medwal, R. S. Rawat, H. Asada, S. Gupta, and Y. Fukuma, "Disentanglement of intrinsic and extrinsic side-jump scattering induced spin Hall effect in N-implanted Pt," *Phys. Rev. B* **107**(6), 064402 (2023).
- <sup>48</sup>Y. Zhao, Q. Song, S.-H. Yang, T. Su, W. Yuan, S. S. P. Parkin, J. Shi, and W. Han, "Experimental investigation of temperature-dependent Gilbert damping in permalloy thin films," *Sci. Rep.* **6**(1), 22890 (2016).
- <sup>49</sup>K. Garello, I. M. Miron, C. O. Avci, F. Freimuth, Y. Mokrousov, S. Blügel, S. Auffret, O. Boulle, G. Gaudin, and P. Gambardella, "Symmetry and magnitude of spin-orbit torques in ferromagnetic heterostructures," *Nat. Nanotechnol.* **8**(8), 587–593 (2013).
- <sup>50</sup>M. Aoki, E. Shigematsu, R. Ohshima, T. Shinjo, M. Shiraishi, and Y. Ando, "Coexistence of low-frequency spin-torque ferromagnetic resonance and unidirectional spin Hall magnetoresistance," *Phys. Rev. B* **104**(9), 094401 (2021).
- <sup>51</sup>J. Zhou, X. Shu, Y. Liu, X. Wang, W. Lin, S. Chen, L. Liu, Q. Xie, T. Hong, P. Yang, B. Yan, X. Han, and J. Chen, "Magnetic asymmetry induced anomalous spin-orbit torque in IrMn," *Phys. Rev. B* **101**(18), 184403 (2020).
- <sup>52</sup>T. Nan, C. X. Quintela, J. Irwin, G. Gurung, D. F. Shao, J. Gibbons, N. Campbell, K. Song, S.-Y. Choi, L. Guo, R. D. Johnson, P. Manuel, R. V. Chopdekar, I. Hallsteinsen, T. Tybell, P. J. Ryan, J.-W. Kim, Y. Choi, P. G. Radaelli, D. C. Ralph, E. Y. Tsymlal, M. S. Rzchowski, and C. B. Eom, "Controlling spin current polarization through non-collinear antiferromagnetism," *Nat. Commun.* **11**(1), 4671 (2020).
- <sup>53</sup>J. E. Hirsch, "Spin Hall effect," *Phys. Rev. Lett.* **83**(9), 1834–1837 (1999).
- <sup>54</sup>A. Bose, N. J. Schreiber, R. Jain, D.-F. Shao, H. P. Nair, J. Sun, X. S. Zhang, D. A. Muller, E. Y. Tsymlal, D. G. Schlom, and D. C. Ralph, "Tilted spin current generated by the collinear antiferromagnet ruthenium dioxide," *Nat. Electron.* **5**(5), 267–274 (2022).
- <sup>55</sup>T. M. Cham, S. Karimeddiny, V. Gupta, J. A. Mittelstaedt, and D. C. Ralph, "Separation of artifacts from spin-torque ferromagnetic resonance measurements of spin-orbit torque for the low-symmetry van der Waals semi-metal ZrTe<sub>3</sub>," *Adv. Quantum Technol.* **5**(2), 2100111 (2022).
- <sup>56</sup>A. Vansteenkiste, J. Leliaert, M. Dvornik, M. Helsen, F. Garcia-Sanchez, and B. Van Waeyenberge, "The design and verification of MuMax<sup>3</sup>," *AIP Adv.* **4**(10), 107133 (2014).
- <sup>57</sup>J. C. Slonczewski, "Current-driven excitation of magnetic multilayers," *J. Magn. Magn. Mater.* **159**(1–2), L1–L7 (1996).
- <sup>58</sup>J. Park, G. E. Rowlands, O. J. Lee, D. C. Ralph, and R. A. Buhrman, "Macrospin modeling of sub-ns pulse switching of perpendicularly magnetized free layer via spin-orbit torques for cryogenic memory applications," *Appl. Phys. Lett.* **105**(10), 102404 (2014).
- <sup>59</sup>M. R. Karim, S. Manna, A. K. Gupta, J. R. Mohan, S. K. Maharana, J. V. Vas, A. Bose, S. Gupta, R. S. Rawat, H. Asada, Y. Fukuma, and R. Medwal, "Observation of out-of-plane spin-orbit torque in a polycrystalline Py/IrMn<sub>3</sub> heterostructure," *Phys. Rev. B* **110**, 245423 (2024).
- <sup>60</sup>J.-W. Xu and A. D. Kent, "Charge-to-spin conversion efficiency in ferromagnetic nanowires by spin torque ferromagnetic resonance: Reconciling lineshape and linewidth analysis methods," *Phys. Rev. Appl.* **14**(1), 014012 (2020).